**PAPER**

Check for updates

# Silver and carbon nitride-doped nickel selenide for effective dye decolorization and bactericidal activity: *in silico* docking study

Muhammad Imran,[a] Ali Haider, [ID] *[b] Anum Shahzadi,[c] Muhammad Mustajab, [ID] [d] Anwar Ul-Hamid, [ID] *[e] Hameed Ullah,[f] Sherdil Khan,[f] Hisham S. M. Abd-Rabboh[g] and Muhammad Ikram [ID] *[d]

In this study, nickel selenide (NiSe), $Ag/C_3N_4$–NiSe, and $C_3N_4/Ag$–NiSe nanowires (NWs) were synthesized *via* coprecipitation. The prepared NWs were employed for the degradation of the rhodamine B (RhB) dye in the absence of light using sodium borohydride ($NaBH_4$), bactericidal activity against pathogenic *Staphylococcus aureus* (*S. aureus*) and *in silico* docking study to investigate the D-alanine ligase (DDl) and deoxyribonucleic acid (DNA) gyrase of *S. aureus*. NWs demonstrate a catalytic degradation efficiency of 69.58% toward RhB in a basic medium. The percentage efficacy of the synthesized materials was evaluated as 19.12–42.62% at low and 36.61–49.72% at high concentrations against pathogenic *S. aureus*. Molecular docking results suggest that both $C_3N_4/Ag$-doped NiSe and $Ag/C_3N_4$-doped NiSe possess inhibitory activities toward DDl and DNA gyrase of *S. aureus*, which coincides with the *in vitro* bactericidal activity. Based on the research outcomes, the synthesized NWs show potential as an effective agent for water purification and resistance to microbial contaminants.

## 1 Introduction

Organic and inorganic pollutants affect freshwater reservoirs and pathogenic microorganisms contaminate foodstuffs, posing significant challenges to maintaining a healthy environment. Microbial contamination is spread by microbes, including bacteria (*S. aureus* and *E. coli*) and viruses (hepatitis A and E viruses).[1,2] *S. aureus* releases a wide range of toxins, including staphylococcal enterotoxins, that cause food poisoning and subclinical mastitis.[3] Mastitis is an infection characterized by the inflammation of the udder tissue in the mammary gland. The inflammation originates from microbial infection, contributing to an economic loss in dairy sectors and causing detrimental effects on milk quality and composition.[4] This is the primary factor leading to a decrease in milk production caused by the damage to mammary tissues and is responsible for 70% of the total cost reductions.[5] Microbial contamination was reduced by numerous materials that emerged as exceptionally effective antibacterial agents, attracting significant attention owing to their extraordinary stability, remarkable physical features, and perceived safety for humans and animals.[6] The antibacterial properties of NiSe NPs have been investigated to control the growth of *S. aureus* and *E. coli* bacteria. NiSe as a catalyst compared to the standard medicine gentamycin shows an inhibition zone of 18 mm against *E. coli* and *S. aureus*. The synthesized materials (5 mL) were used as an antimicrobial agent against *E. coli* and *S. aureus* and exhibit inhibition zones of 10 mm and 15 mm, respectively.[7]

Organic and inorganic pollutants, including dyes (methylene orange, methylene blue (MB), and rhodamine B (RhB)) and heavy metals (Cd, Pb, As, Hg, and Cr), are primary contaminants causing water pollution.[8] Cationic synthetic dyes are regarded as exceptionally hazardous color dyes released into water reservoirs and pose significant hazards to environmental stability.[9] RhB is a synthetic organic and non-biodegradable dye frequently employed in the food, textile, and paper industries. RhB has the potential to pollute the environment, causing several detrimental infections in both humans and animals, including eye irritation, skin irritation, and respiratory diseases.[10] To address these issues, several methods have been

*[a]Department of Chemistry, Government College University Faisalabad, Pakpattan Road, Sahiwal, Punjab, 57000, Pakistan*

*[b]Department of Clinical Sciences, Faculty of Veterinary and Animal Sciences, Muhammad Nawaz Shareef University of Agriculture, Multan 66000, Punjab, Pakistan*

*[c]Department of Pharmacy, COMSATS University Islamabad, Lahore Campus, 54000, Pakistan*

*[d]Solar Cell Applications Research Lab, Department of Physics, Government College University Lahore, Lahore 54000, Punjab, Pakistan. E-mail: dr.muhammadikram@gcu.edu.pk*

*[e]Core Research Facilities, King Fahd University of Petroleum & Minerals, Dhahran 31261, Saudi Arabia*

*[f]Laboratory of Nanomaterials for Renewable Energy and Artificial Photosynthesis (NanoREAP), Institute of Physics, UFRGS, 91509-900 Porto Alegre, Rio Grande do Sul, Brazil*

*[g]Chemistry Department, College of Science, King Khalid University, P. O. Box 9004, Abha 62223, Saudi Arabia*

employed, including chlorination, electrochemical degradation, ion exchange, adsorption, photocatalysis, and catalysis, for the degradation of organic and inorganic dyes. Most of these methods are expensive, require complicated equipment, and produce non-reusable products.[11,12] Among these methods, catalytic degradation is highly efficient in terms of energy consumption, ecological friendliness, economic viability, and ability to eliminate or break down harmful pollutants.[13]

Various metal selenides such as CdSe, ZnSe, PbSe, CuSe, HgSe, and $NiSe_3$ have been commonly used for the degradation of the dye.[7,14] Among these, nickel selenide (NiSe) has garnered considerable attention owing to its distinctive and remarkable magnetic and electrical properties for a wide range of applications, such as supercapacitors,[1] optics,[15] solar cells, sensors, electrocatalysis,[16] and photocatalysis.[14] NiSe exhibits notable capabilities, including an appropriate band gap energy, cost-effectiveness, chemical stability, nontoxicity, and outstanding catalytic performance.[17] The catalyst performance can be improved by doping *via* various chemical substances such as noble metals (*e.g.*, Ag, Au, Pd, and Pt) and carbon-based materials (carbon nanotubes, carbon nitride ($C_3N_4$), and graphene oxide).[18,19] The noble metals and carbon-based catalysts have a large specific surface area and effectively separate photo-generated charge carriers, leading to the degradation of the organic dye.[20] Silver (Ag) was extensively used in the synthesis of hybrid semiconductor materials to enhance the efficiency of carrier separation and promote ecological sustainability for dye degradation.[21]

Two-dimensional carbon-based materials are composed of carbon atoms and have numerous nitrogen-rich functional groups. $C_3N_4$ exhibits various noteworthy characteristics including electronic delocalization properties, sustainable nature, uncomplicated preparation technique, non-toxicity, excellent thermal and chemical durability, and convenient accessibility.[22,23] The metal–semiconductor interactions capture electrons and enhances the separation of electron–hole pairs, thereby improving the degradation of the dye. A hydrothermal technique was used to synthesize NiSe and silver phosphate composite, which demonstrated a degradation efficiency of more than 80% in just 20–30 minutes.[24]

In this research, cost-effective coprecipitation approach has been used to synthesize NiSe, $Ag/C_3N_4$ and $C_3N_4$/Ag-doped NiSe nanowires (NWs). These NWs were used to investigate the catalytic efficiency for the degradation of RhB dye and antibacterial efficacy against pathogenic bacteria *S. aureus*. The study's findings establish the superiority of carbon-based materials and metal-doped materials over single-component materials.

## 2 Experimental part

### 2.1. Materials

Hydrazine hydrate ($N_2H_4$, 50–60%), silver nitrate ($AgNO_3$, 99.8–100%), selenium powder (Se, 99.5%), and urea ($CH_4N_2O$) were procured from Sigma-Aldrich. Nickel nitrate hexahydrate ($Ni(NO_3)_2 \cdot 6H_2O$) was procured from VWR Chemicals.

### 2.2. Preparation of reagents

**2.2.1. Synthesis of carbon nitride.** Carbon nitride was synthesized through the pyrolysis of urea at 550 °C for 120 minutes. A dirty yellow-color material was produced, which confirmed the synthesis of $C_3N_4$ (Fig. 1(a)).

**2.2.2. Preparation of selenium solution.** 0.6 M of selenium (1.2 g) solution was prepared using deionized water (DI water) under ultra-sonication for 10 minutes.

### 2.3. Synthesis of ternary system

**2.3.1. Synthesis of NiSe.** 0.6 M of $Ni(NO_3)_2 \cdot 6H_2O$ (4.47 g) was prepared using DI water (25 mL) with continuous stirring and heating at 120 °C for 10 minutes. The prepared solutions of selenium and $Ni(NO_3)_2 \cdot 6H_2O$ were mixed to prepare NiSe with continuous stirring and heating at 120 °C for 10 minutes, and the pH of the solution was maintained up to 10 using the required concentration of hydrazine hydrate. The colloidal solution was stirred and heated constantly at 120 °C for 60 minutes to prepare a homogeneous solution. The stirred solution was washed to remove the impurity with DI water using centrifugation at 7000 rpm for 8 minutes. The obtained solution was heated overnight at 150 °C to sustain the fine powder (Fig. 1(b)).

**2.3.2. Synthesis of $Ag/C_3N_4$ and $C_3N_4$/Ag-doped NiSe.** To synthesize $Ag/C_3N_4$-doped NiSe, the above prepared homogeneous colloidal solution of NiSe was doped with a fixed amount of Ag and $C_3N_4$ (0.17 g) under constant stirring and heating at 120 °C for 60 minutes, and the pH of the $Ag/C_3N_4$-doped NiSe solution was maintained up to 10. The stirred solution was washed with DI water using centrifugation for 8 minutes. The washed solution was heated overnight at 150 °C to sustain the
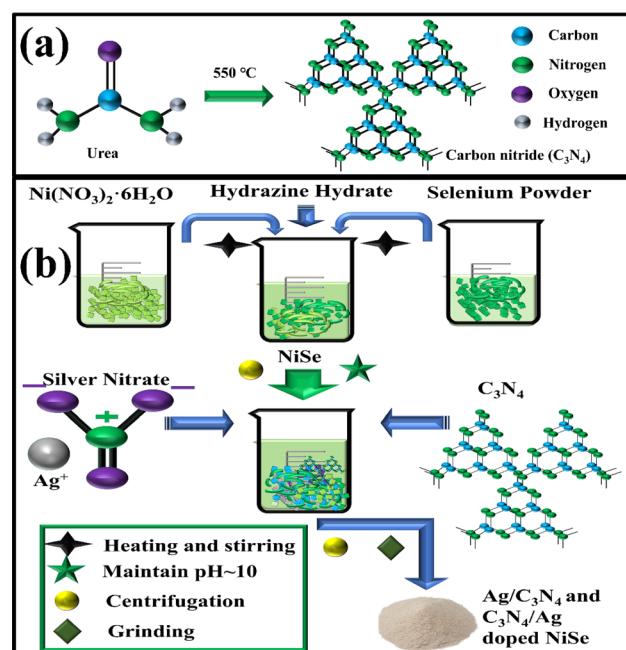


**Fig. 1** Schematic of the synthesis of (a) $C_3N_4$, (b) NiSe, $Ag/C_3N_4$ and $C_3N_4$/Ag-doped NiSe.

fine powder. To synthesize $C_3N_4$/Ag-doped NiSe, the route mentioned above was adopted, in which a fixed concentration of Ag and $C_3N_4$ was used to incorporate in NiSe (Fig. 1(b)).

## 2.4. Catalytic activity (CA)

The catalytic efficiency of NiSe, Ag/$C_3N_4$ and $C_3N_4$/Ag-doped NiSe was evaluated for the degradation of RhB dye. The chemical reagents RhB and sodium borohydride ($NaBH_4$) were freshly synthesized to guarantee the purity of the outcomes. RhB solution ($10 \text{ mg L}^{-1}$) was prepared and separated into three equal parts to achieve different pH levels corresponding to basic (pH $\sim$ 12), neutral (pH $\sim$ 7), and acidic (pH $\sim$ 4) media. A combined solution of 3 mL of RhB and 400 μL of $NaBH_4$ was prepared. In addition, 400 μL of the synthesized NWs were added to the above mentioned solution to investigate the degradation of the dye. NWs (as a catalyst) were used to decrease the activation energy and improve the efficiency of catalysis. Spectrophotometric techniques were used to determine the absorption variation spectra with a UV-Vis spectrophotometer conducted at regular intervals of time. The RhB molecule exhibits an absorption peak at a precise wavelength of 554 nm. The RhB molecule experienced a reduction reaction in which the color changed from pink to nearly colorless. The degradation was measured utilizing eqn (1).[25]

$$\% \text{ degradation} = (C_o - C_t)/C_o \times 100 \tag{1}$$

## 2.5. Isolation and identification of S. aureus

**2.5.1. Sample collection and isolation.** Bovine milk was collected from veterinary hospitals and farms in the public sectors in Punjab, Pakistan. The milk samples were cultivated on 5% sheep blood agar and incubated at room temperature (37 °C) for 24–48 hours. The typical isolate of *S. aureus* was purified, and colonies of *S. aureus* were collected and streaked in triplets on mannitol salt agar (TM Media, Titan Biotech Ltd, India) for the growth of bacteria.

**2.5.2. Identification of MDR *S. aureus*.** In Bergey's manual of determinative bacteriology, the identification of bacterial colonies was accomplished by biochemical techniques such as Gram staining test (catalase and coagulase test). The disc diffusion test is based on the standards established by the National Committee for Clinical Laboratory Standards (NCCLS) for the separation of multidrug-resistant *Staphylococcus aureus* to assess the antibiotic susceptibility of typical colonies. The antibiotic discs including gentamicin (10 μg), tylosin (30 μg), oxytetracycline (30 μg), trimethoprim + sulphamethoxazole (1.25 μg + 23.75 μg), and ciprofloxacin (5 μg) were prepared using Mueller–Hinton agar (MHA) (TM Media, Titan Biotech Ltd, India). The discs were incubated at 37 °C for 24 hours.[26] Bacteria were discovered to be resistant to different antibiotics that were classified as MDR.[27]

**2.5.3. Antimicrobial activity.** The agar well diffusion method was employed to conduct the *in vitro* antimicrobial potential of NWs on 10 typical isolates of MDR *S. aureus* that were recovered from mastitis milk samples. 0.5 McFarland standard ($1.5 \times 10^8$ colony-forming units per mm) of MDR *S. aureus* was swabbed onto Petri dishes. A sterile cork borer was used to drill the wells with a diameter of 6 mm. The low (0.5 mg/ 50 μL) and high (1.0 mg/50 μL) concentrations of NWs were utilized to conduct the antimicrobial test for measuring the inhibition zones. Ciprofloxacin concentration (0.005 mg/50 μL) was employed as a positive control, and DI water (50 μL) served as a negative control.

**2.5.4. Statistical analysis.** The efficacy of the antimicrobial activity was evaluated by measuring the diameter of the inhibition zone in mm. A statistical evaluation of the inhibition zone measurements was investigated using Statistical Package for Social Sciences (SPSS) Version 20.0, specifically employing one-way analysis of variance (ANOVA).

## 2.6. Molecular docking analysis

The enhanced antibacterial capabilities of the synthesized compounds, namely, $C_3N_4$/Ag-doped NiSe and Ag/$C_3N_4$-doped NiSe, prompted an investigation into the enzyme-binding affinity of these compounds to DDl and DNA gyrase from *S. aureus* along with their binding potential inside their respective active pockets. DNA gyrase is particularly notable among type II topoisomerases because it has the ability to generate negative supercoils in closed circular DNA. Antibiotics have been developed to inhibit DNA gyrase, a crucial enzyme exclusive to prokaryotes.[28] DDl, an additional enzyme involved in the production route of the cell wall, has become a promising target for the development of novel antibiotics. The reaction facilitated by the DDl enzyme generates the precursor of the cell wall peptidoglycan, known as D-alanine:D-alanine dipeptide. This reaction consists of two half-reactions: the first one utilizes an ATP molecule and a D-alanine substrate, while the second one requires an additional D-alanine substrate to finalize the process.[29] The protein data bank was used to acquire the structural coordinates of specific enzyme targets with accession codes 2I8C[28] and 5CPH[29] for DDI$_{S. aureus}$ and DNA gyrase$_{S. aureus}$, respectively. The molecular docking experiment was carried out using SYBYL-X 2.0.[30,31] The 3D structures were built using the Sybyl-X 2.0 program's SKETCH module, and the energy was minimized using the Tripos force field with Gasteiger–Hückel atomic charges.[32] The Surflex-Dock module was used to investigate the interactions between NWs and active site residues of certain proteins. In addition, any missing hydrogens were introduced. The AMBER 7 FF99 force field was utilized to enhance atomic charges. Using the Powell approach with a convergence gradient of 0.5 kcal (mol Å)$^{-1}$ over 1000 cycles successfully reduces the energy and prevents steric conflicts. The ligand–receptor complexes were assessed using consensus scoring (C-score), an empirical consensus scoring approach based on hammerhead's scoring system. The system used many scores, including the chem-score, crash score, dock-score (D-score), gold score (G-score), polar score, and potential mean force (PMF) score. The evaluation process involved using a molecular similarity method, specifically morphological similarity, to generate and rank potential positions of ligand fragments. The docking was performed with the SYBYL-X 2.0

software. In line with a previous investigation, the SYBYL-X 2.0 software was used to generate three-dimensional conformations of compounds and evaluate the binding affinities of NWs with the amino acid residues located in the binding sites of specific proteins.

### 2.7. Characterization techniques

The phase information and crystal structure of the synthesized NWs in the $2\theta$ range of 20–65° were investigated using a PANalytical X'Pert PRO X-ray diffraction (XRD) instrument with Cu K$\alpha$ radiation ($\lambda = 1.540$ Å). The presence of functional groups in the FTIR spectra was detected using a PerkinElmer spectrometer. A UV-Vis spectrophotometer (LabDex) was used to determine the optical characteristics in the range of 250–450 nm. The surface morphology and elemental composition of the prepared NWs were investigated using a JSM-6460LV FE-SEM system. The morphology of the internal structure of the prepared NRs was examined using a JEOL JEM 2100F TEM equipment from KFUPM, Saudi Arabia.

## 3 Results and discussion

### 3.1. XRD analysis

XRD analysis was conducted to investigate the various phases and crystallographic structures of the synthesized NiSe, Ag/C$_3$N$_4$ and C$_3$N$_4$/Ag-doped NiSe (Fig. 2(a)). The characteristic diffraction peaks observed at $2\theta$ values of 31.9°, 38.1°, 43.8°, 45.2°, 55.8° and 61.9° ascribed to the (042), (133), (135), (028), (119) and (172) planes of orthorhombic crystal structure of NiSe

phase matched with JCPDS card # 00-029-0935. The diffraction peaks observed at a $2\theta$ value of 22.3°, 25.2°, 27.0°, 33.4°, 41.3°, 50.9°, and 51.9° were indexed to (122), (132), (201), (114), (163), (281) and (264), the planes of the orthorhombic crystal structure of Ni$_6$Se$_5$ with the space group $Pca2_1$, well matching with the JCPDS # 00-029-0934. The prominent diffraction peaks that occurred at $2\theta$ values if 23.4° and 29.9° are in agreement with the diffraction planes (110) and (020) of an orthorhombic crystal structure of NiSe$_2$, respectively. The crystal structure is classified under the space group $Pnnm$ and agrees with the JCPDS # 00-018-0886. The peak intensity increases as the concentration of the dopants increases, attributed to the Ag plasmonic effects and the effective dispersion of Ag@C$_3$N$_4$.[33] The sharp and intense peaks of the product were revealed upon the addition of Ag/C$_3$N$_4$ and C$_3$N$_4$/Ag, evidenced by their crystalline nature.[34]

**3.1.1. Crystallite size.** The crystallite (grain) size of the synthesized NWs was measured using the Debye–Scherrer formula (2).[35]

$$GS = \frac{k\lambda}{\beta \cos \theta} \tag{2}$$

The grain size (GS) of NiSe, Ag/C$_3$N$_4$ and C$_3$N$_4$/Ag-doped NiSe was calculated to be 20.35, 19.48, and 16.90 nm, respectively.

**3.1.2. Surface area.** Eqn (3) was utilized to determine the surface area of the NWs.[36]

$$\text{Surface area} = \frac{6000}{GS \times \rho_x} \tag{3}$$
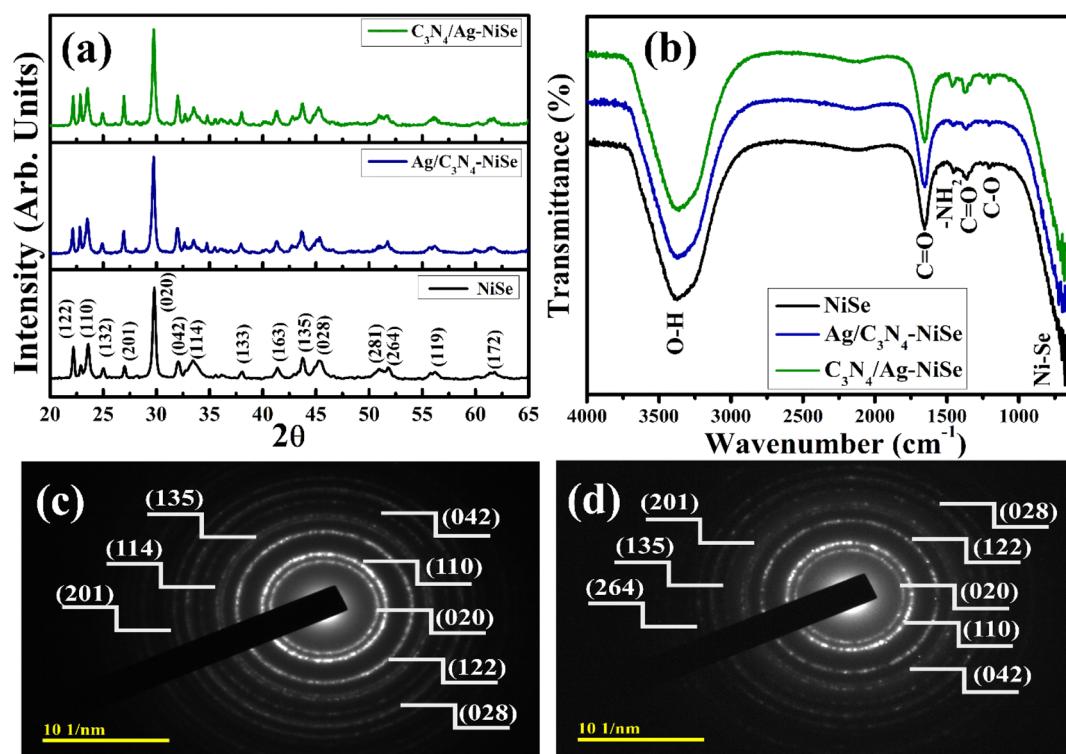


Fig. 2 (a) X-ray diffraction pattern, (b) FTIR spectra and (c and d) SAED images of NiSe and Ag/C$_3$N$_4$-doped NiSe.

The surface area of NiSe, Ag/$C_3N_4$ and $C_3N_4$/Ag-doped NiSe was measured to be 40.95, 44.00, and 50.72 $m^2\,g^{-1}$, respectively. The surface-to-volume ratio and specific surface area increased as the crystallite size decreased and *vice versa*.[37]

**3.1.3. Porosity.** The % porosity of undoped, Ag/$C_3N_4$ and $C_3N_4$/Ag-doped NiSe NWs was examined using the formula (4)[38]

$$\% \text{ porosity} = \left[1 - \frac{\rho_b}{\rho_x}\right] \times 100 \qquad (4)$$

where $\rho_x$ and $\rho_b$ are the X-ray density and bulk density of the synthesized materials. The % age porosity of NiSe, Ag/$C_3N_4$ and $C_3N_4$/Ag-doped NiSe were measured as 4, 33.6, and 34.1%, respectively.

### 3.2. FTIR analysis

FTIR analysis was used to examine the presence of various chemical structures and functional groups for NiSe, Ag/$C_3N_4$ and $C_3N_4$/Ag-doped NiSe in the frequency range of 4000–500 $cm^{-1}$, depicted in Fig. 2(b). The band observed at 1658 $cm^{-1}$ was attributed to the stretching vibration of the C=O and weak O–H band of water molecules. Additionally, the bending vibration of the O–H recorded at 3381 $cm^{-1}$ is assigned to the absorption of water molecules on the surface of individual atoms of NiSe.[39] The band observed at 1460 $cm^{-1}$ was assigned to the vibration of –$NH_2$ of hydrazine hydrate.[40] The stretching vibration band observed at 1368 $cm^{-1}$ was attributed to the presence of the carbonyl (C=O) group absorbed from the atmospheric carbon dioxide ($CO_2$).[41] The spectral band observed at 1217 $cm^{-1}$ is associated with the stretching vibrations of C–O.[15] The bands observed in the range of 850 to 500 $cm^{-1}$ are associated with the vibrational modes of nickel (Ni) and selenium (Se) in NiSe.[7] The incorporation of Ag/$C_3N_4$ and $C_3N_4$/Ag to NiSe showed a band shift towards the lower wavenumber corresponding to the vibrations of Ni–Se bonds. SAED analysis was used to conduct the single and polycrystalline nature of the synthesized NiSe and Ag/$C_3N_4$-doped NiSe NWs (Fig. 2(c) and (d)). Bright circular rings exhibit the impression of the polycrystalline nature of NWs. The coherence of the indexed rings with the XRD crystalline plane is in agreement with the XRD findings.

### 3.3. Raman analysis

To examine the vibrational, rotational, and structural characteristics of NiSe, Ag/$C_3N_4$ and $C_3N_4$/Ag-doped NiSe, they were investigated in the range of 90–500 $cm^{-1}$ using Raman spectroscopy (Fig. 3(a)). The observed peaks in the lower wavelength are attributed to the vibration of $A_g$ and $T_g$ modes of NiSe.[42] The lower frequency band appears at 113 $cm^{-1}$ assigned to the lattice translation of hydrazine hydrate.[43] The band observed at 238 $cm^{-1}$ is assigned to the out-of-plane $A_{1g}$[44] vibration mode of elemental selenium configuration and specifically describes the tensile modes of the Se–Se bonds.[45,46] Raman spectra reveal the specific bands of $T_g$ at about 141 and 255 $cm^{-1}$, attributed to the vibrational modes of Se–Se.[45,47] A small shifting was observed in the Raman spectra upon the incorporation of Ag/$C_3N_4$ and $C_3N_4$/Ag. The chemical structure and interaction observed in the Raman spectra coincide with the functional group analysis and chemical structure of NWs determined by FTIR.

### 3.4. UV-visible spectroscopy

The optical properties of NiSe, Ag/$C_3N_4$ and $C_3N_4$/Ag-doped NiSe were investigated through UV-Vis spectroscopy in the wavelength range of 250–450 nm (Fig. 3(b)). The absorption spectra of NiSe and Se exhibited strong absorption peaks at 298 and 390 nm, respectively.[48–50] The reduction in the absorption peak intensity at about 390 nm demonstrates a potential change in the composition and properties of NWs. Doped NiSe showed a peak shift that could be due to the quantum confinement effect.[48] The intrinsic absorption shift is attributed to a decrease in energy, which indicates that the electrical conductivity of NiSe is enhanced through doping.[51] The band gap energy was calculated from the maximum absorption spectra. The measured optical band gap was 4.16, 4.06, and 4.09 eV for undoped, Ag/$C_3N_4$ and $C_3N_4$/Ag-doped NiSe NWs, respectively. The energy band gap of the additionally observed optical absorption edge at 390 nm was measured as 3.17 eV.
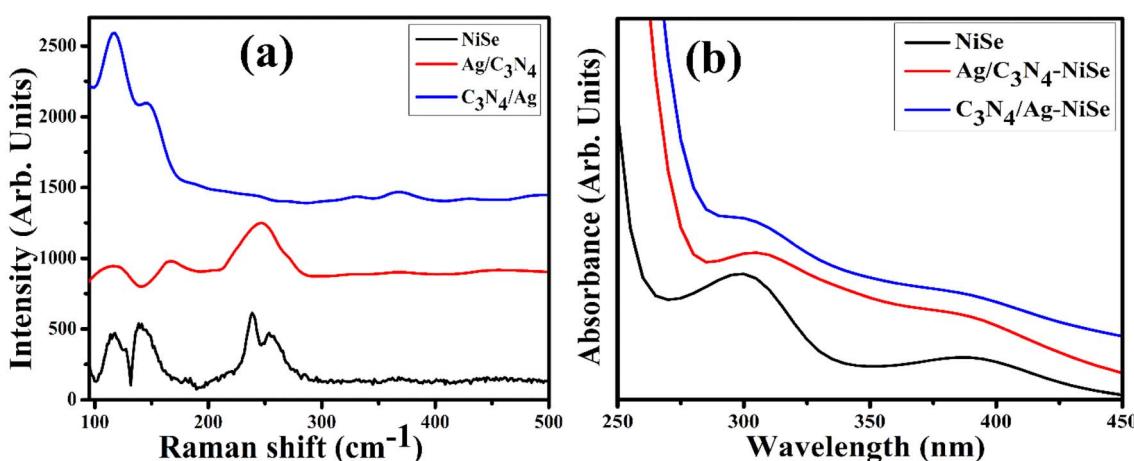


**Fig. 3** (a) Raman spectra and (b) optical absorbance spectra of NiSe, Ag/$C_3N_4$ and $C_3N_4$/Ag-doped NiSe NWs.
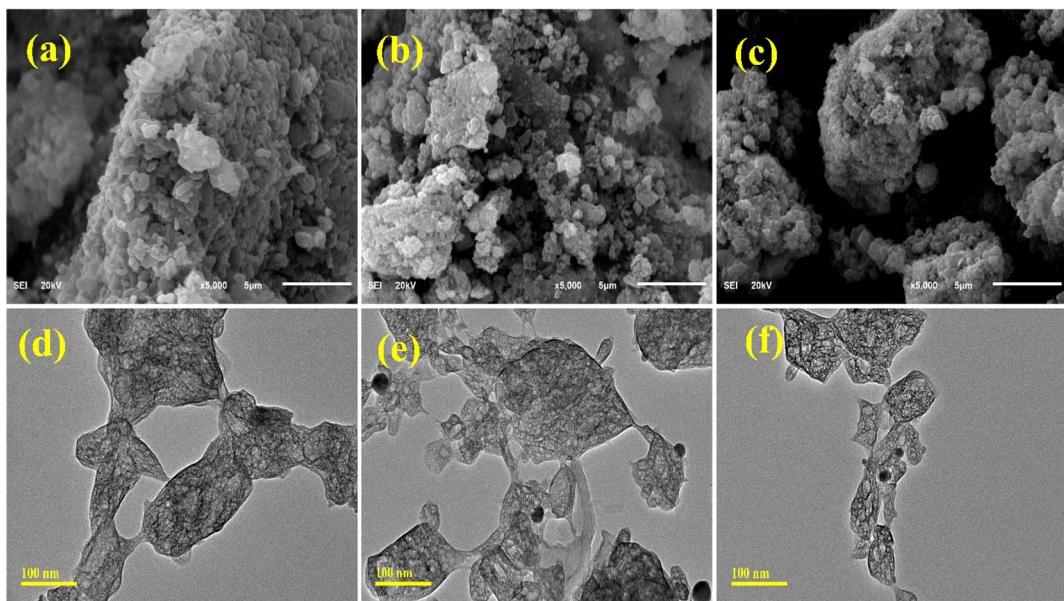
Fig. 4   Structure and surface morphology of NiSe, Ag/C$_3$N$_4$ and C$_3$N$_4$/Ag-doped NiSe (a–c) SEM analysis and (d–f) TEM analysis.

### 3.5.   SEM analysis

SEM micrographs were used to identify the surface morphology of the synthesized NiSe, Ag/C$_3$N$_4$ and C$_3$N$_4$/Ag-doped NiSe, as represented in Fig. 4(a)–(c). NiSe revealed the agglomerated irregular sheet-like morphology arranged in layers. Ag/C$_3$N$_4$ and C$_3$N$_4$/Ag-doped NiSe NWs exhibit a decrease in agglomeration and the formation of chunk-like cluster morphology. The surface area and active sites of materials are enhanced,

resulting in a reduction of agglomeration. The larger surface area and the presence of numerous active sites are attributed to higher catalytic efficiency.[52]

### 3.6.   TEM analysis

TEM analysis was used to investigate the topography and structural morphology of the prepared materials, as presented in Fig. 4(d)–(f). NiSe indicates the agglomeration resulting in
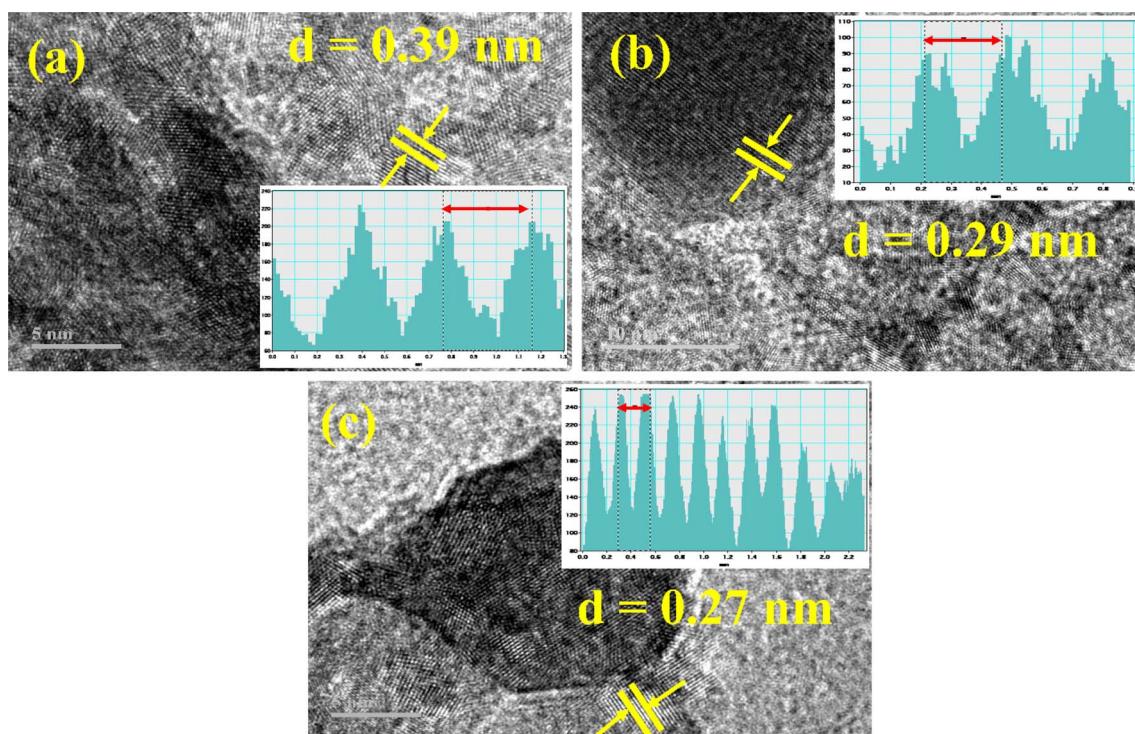


Fig. 5   The interlayer *d*-spacing of synthesized NWs (a) NiSe, (b) Ag/C$_3$N$_4$-doped NiSe, and (c) C$_3$N$_4$/Ag-doped NiSe.
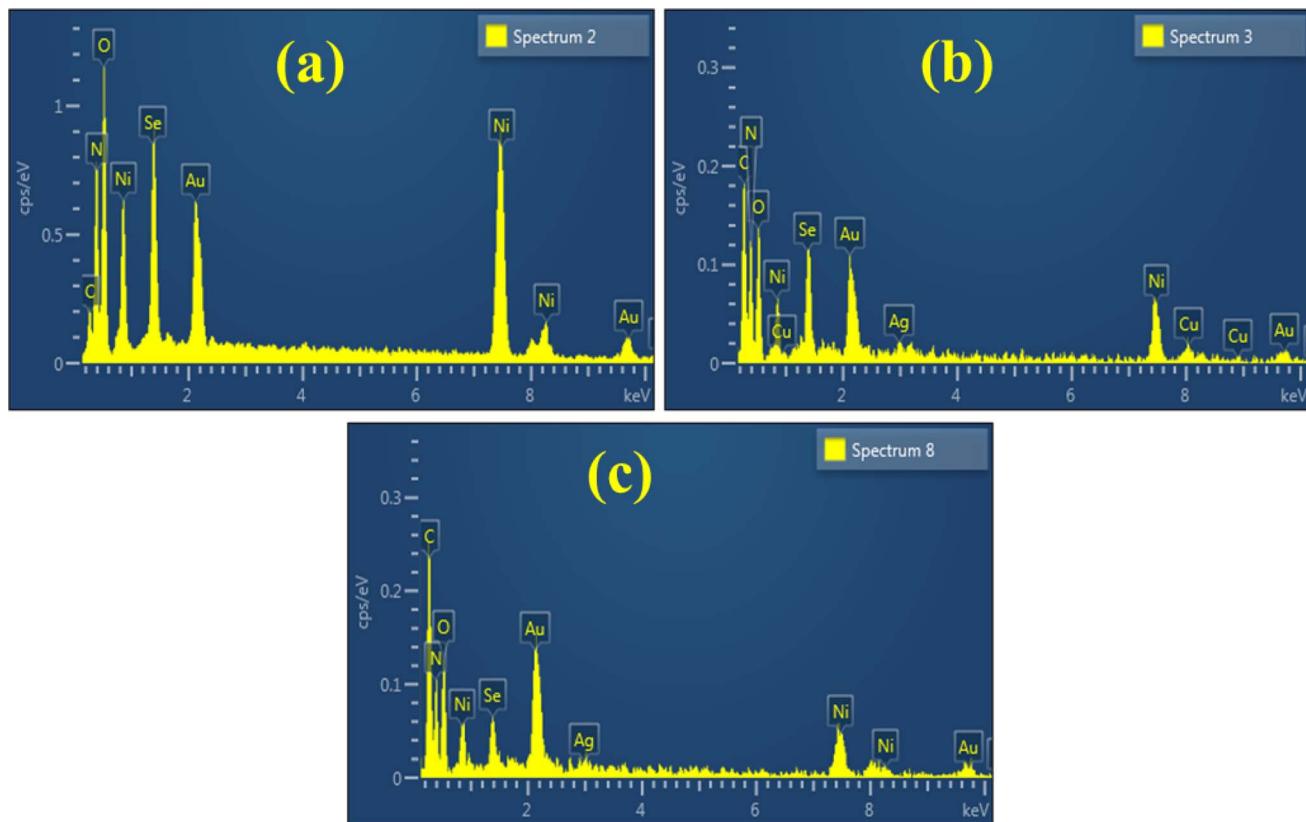
**Fig. 6** Elemental composition of (a) NiSe, (b) Ag/$C_3N_4$-doped NiSe, and (c) $C_3N_4$/Ag-doped NiSe.
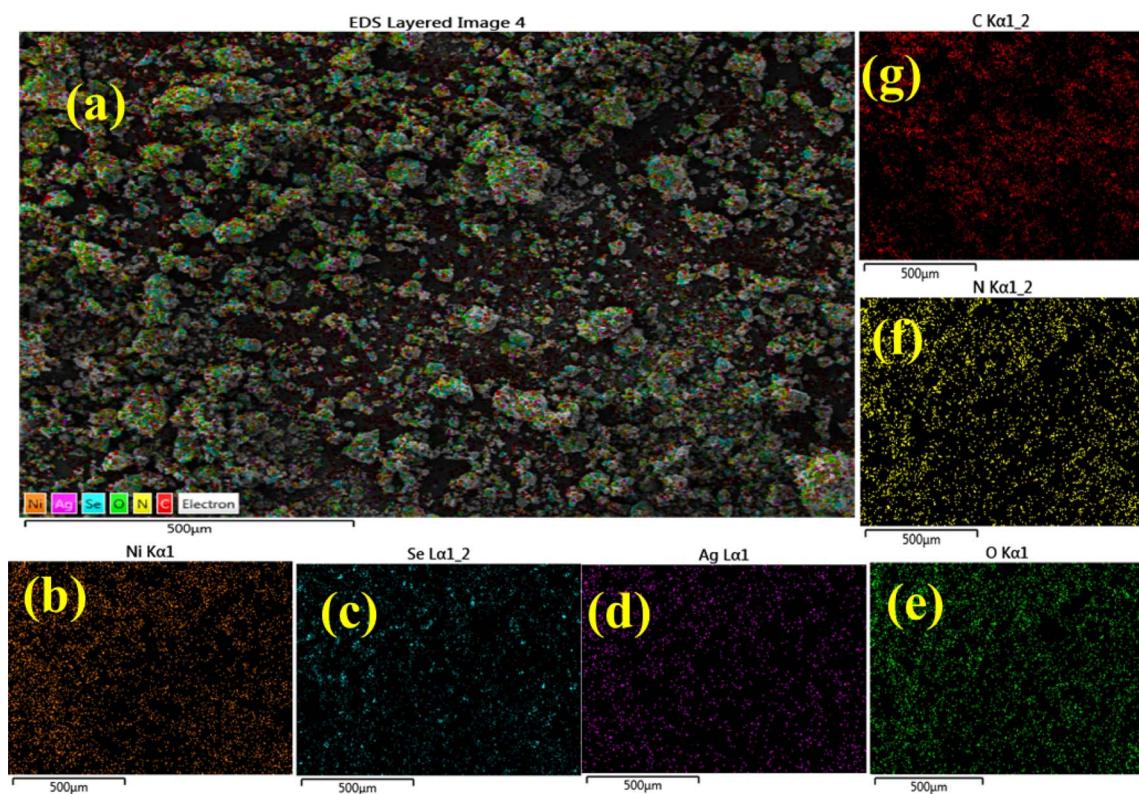


**Fig. 7** Elemental mapping analysis of (a) $C_3N_4$/Ag-doped NiSe (b) Ni, (c) Se, (d) Ag, (e) O, (f) N, and (g) C atoms.

**Paper**

the formation of chunk and cluster-like morphologies. The observed morphology consists of interconnected arrays of clusters, which are agglomerated with chains of nanowires (NWs) in a complicated manner. Ag/C$_3$N$_4$-doped NiSe exhibits a reduction in the agglomeration, in which the cluster of chunks is connected through a wire-like morphology. C$_3$N$_4$/Ag-doped NiSe revealed a reduction of agglomeration and NWs appeared in the cluster of chunks.

### 3.7. Interlayer *d*-spacing

The interlayer *d*-spacing of undoped, Ag/C$_3$N$_4$ and C$_3$N$_4$/Ag-doped NiSe was investigated with the help of Gatan digital software using the HRTEM micrograph shown in Fig. 5(a)–(c). The interlayer *d*-spacing was measured as 0.39, 0.29, and 0.27 nm for NiSe, Ag/C$_3$N$_4$ and C$_3$N$_4$/Ag-doped NiSe, respectively. The measured *d*-spacing is compatible with the XRD measurements.

### 3.8. EDS analysis

The elemental composition of synthesized pure, Ag/C$_3$N$_4$ and C$_3$N$_4$/Ag-doped NiSe was investigated using EDS analysis. The appearance of nickel (Ni), selenium (Se), Ag, oxygen (O),

nitrogen (N), copper (Cu), and gold (Au) in the EDS spectra confirm the successful synthesis of NiSe and doped NiSe (Fig. 6(a)–(c)). The existence of O peaks indicates the impurity as the experiment was performed in open air. The presence of Ag, C, and N atoms suggests the incorporation of Ag and C$_3$N$_4$ in NWs. Cu peaks are associated with the utilization of Cu tape in a sample holder. The appearance of Au peaks is related to the Au coating to reduce the charging effect.

### 3.9. Mapping

Elemental mapping analysis was employed to examine the distinct color representation of different atoms in pure, Ag/C$_3$N$_4$ and C$_3$N$_4$/Ag-doped NiSe NWs. The various color images show the presence of elements Ni, Se, O, Ag, C, and N involved in the Ag/C$_3$N$_4$ and C$_3$N$_4$/Ag-doped NiSe NWs (Fig. 7(a)–(g)).

### 3.10. Catalytic degradation

The degradation of RhB dye was investigated using a UV-visible spectrophotometer (absorption mode). The obtained results of RhB decolorization under acidic, neutral, and alkaline (basic) media are shown in Fig. 8(a)–(c). NiSe, C$_3$N$_4$/Ag and Ag/C$_3$N$_4$-doped NiSe were used as catalysts to speed up the reaction. The
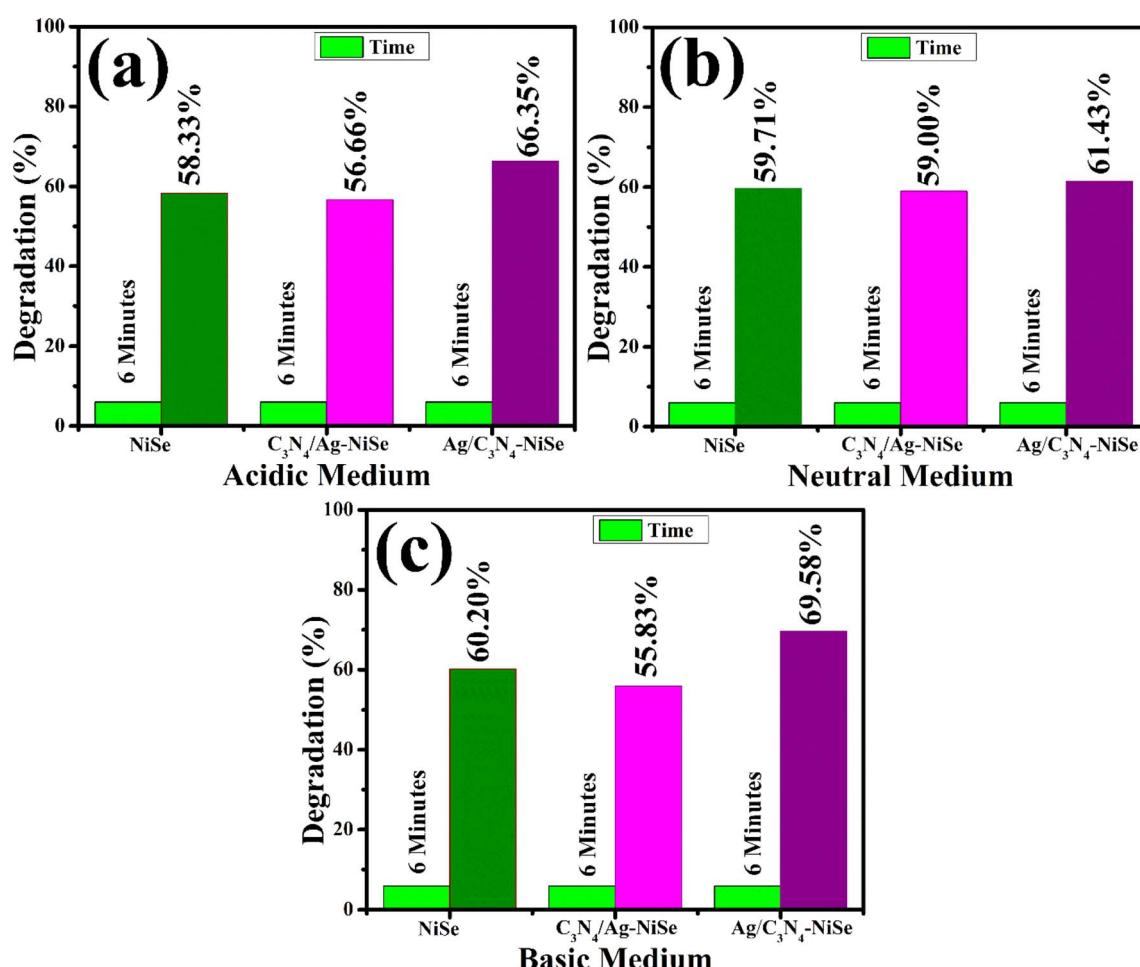


Fig. 8   RhB degradation using synthesized NWs in (a) an acidic medium, (b) neutral medium, and (c) basic medium.

pH has a substantial impact on the degree of dye degradation because the dye waste is discharged at various pH levels. In an acidic medium, 0.5 M of $H_2SO_4$ was added to the RhB solution to maintain a pH $\sim$ 4. A 400 $\mu$L solution of NWs and $NaBH_4$ was added to a 3 mL concentration of RhB dye. The pure, $C_3N_4/Ag$ and $Ag/C_3N_4$-doped NiSe exhibited a degradation efficiency of 58.33%, 56.66%, and 66.35%, respectively, in an acidic medium, as shown in Fig. 8(a). The percentage degradation in neutral (pH $\sim$ 7) medium was measured as 59.71, 59.0, and 61.43%, respectively, as indicated in Fig. 8(b). The morphology of the synthesized materials as NWs can influence the catalytic degradation of the dye by surface-to-volume ratio, surface area, and porosity. The surface area increased, confirmed by XRD, which led to catalytic degradation. A decrease in the catalytic efficacy was observed in the natural and acidic media attributed to the presence of a large surface area of a synthesized catalyst that may prevent the reactants from diffusing to the active sites.[53] The larger surface area has a higher concentration of active sites on the surface of the catalyst. The % age degradation efficiency was reduced due to the less number of active sites in comparison to the number of dye molecules present on the surface of the catalyst.[54] The result obtained from the current study was compared to previous investigations for the degradation of dye, concisely presented in Table 1.

To elucidate the degradation of dye molecules in a basic medium, 0.5 M of NaOH was used to maintain the pH at $\sim$12. The undoped, $C_3N_4/Ag$ and $Ag/C_3N_4$-doped NiSe NWs experienced degradation of 60.20, 55.83, and 69.58%, respectively. Significant degradation was observed in the basic medium attributed to the large surface area of $Ag/C_3N_4$-doped NiSe (Fig. 8(c)). The catalytic degradation of dye in the basic medium decreased upon the incorporation of $C_3N_4/Ag$, which may prevent the reactants from diffusing to active sites. Upon the

insertion of $Ag/C_3N_4$, the surface area of the catalyst was increased, and the reactant diffused into the active sites of the catalyst increased the degradation of the dye. The incorporation of Ag acts as an electron pool and promotes the active species owing to the surface plasmon resonance effect of Ag, leading to an increase in dye degradation.[33] Moreover, in the case of $C_3N_4/Ag$, the surface plasmon effect of Ag was reduced, indicating a decrease in the % age degradation of the dye. The oxidation–reduction reaction takes place in a basic medium between the cationic RhB dye and catalyst that enables the breakdown of the dye molecules into $CO_2$ and water.[58]

Catalytic degradation mechanism involves the reactants ($NaBH_4$ and RhB) and synthesized catalysts (NWs) for the degradation of the dye. $NaBH_4$ reacts with RhB on the surface of the catalyst, resulting in the transfer of electrons to dye molecules. Dye accepts these electrons and its color changes from pink to colorless. The color change signifies the breakdown of the interconnected xanthene ring in the molecular composition of RhB.[59] The mass-to-charge ratio ($m/z$) of 268 and 254 were linked to the $N$-deethylation degradation of the dye.[60] These intermediates possess the capacity to undergo further degradation, leading to the production of smaller products distinguished by $m/z$ values of 148, 118, and 104.[61] The breakdown and conversion of small molecules of the dye lead to the production of $CO_2$, $H_2O$, and various inorganic compounds (Fig. 9).

### 3.11. Antibacterial activity

The antibacterial efficacy of NiSe, $Ag/C_3N_4$ and $C_3N_4/Ag$-doped NiSe NWs was evaluated through the agar well diffusion method. The zone of inhibition against MDR *S. aureus* was determined using a Vernier caliper. Low concentrations (0.5 mg/50 $\mu$L) of synthesized materials exhibit inhibition zone

**Table 1** Literature comparison with the current study for the degradation of the dye

| Samples | Synthesis method | Dyes | Conditions and time | % efficiency | Ref. |
|---|---|---|---|---|---|
| $NiSe_2/g$-$C_3N_4$ | Hydrothermal method | Reactive black 5 | Natural sunlight for 120 minutes | 86.4% | 17 |
| $NiSe_2/BiVO_4$ | Solvothermal method | RhB | Visible light irradiation for 180 minutes | 80% | 55 |
| $NiSe/g$-$C_3N_4$ | Hydrothermal method | Oxytetracycline (OTC) | Visible light irradiation for 60 minutes | 98.68% | 56 |
| $NiSe/g$-$C_3N_4$ | Hydrothermal method | MB | UV lamp for 60 minutes | 92.5% | 56 |
| $rGO/NiSe_2$ | Hydrothermal method | RhB | Visible light irradiation for 120 minutes | 98.8% | 57 |
| $Ag/C_3N_4$–NiSe | Coprecipitation | RhB | Dark using $NaBH_4$ for 6 minutes | 69% | Present work |
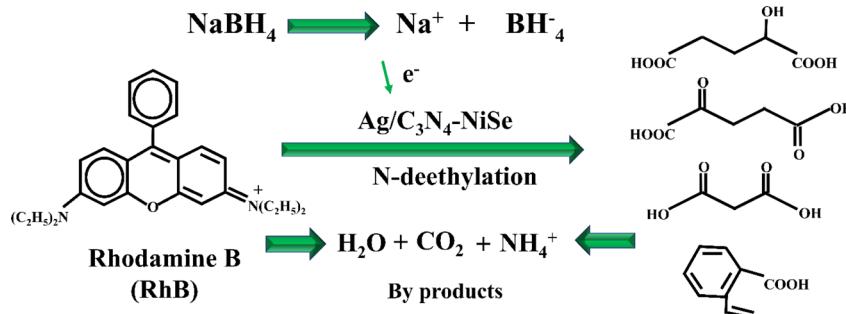


**Fig. 9** Schematic illustration of the catalytic mechanism for the degradation of the RhB dye.

© 2024 The Author(s). Published by the Royal Society of Chemistry

Paper

RSC Advances

ble

measurement in the range of 1.75–3.90 mm, while at high concentrations (1.0 mg/50 μL), a range of 3.35–4.55 mm is provided in Table 2. Ciprofloxacin was used as a positive control to produce inhibitory zones of 9.15 mm against MDR S. aureus. DI water was used as a negative control and does not affect bacterial cells, resulting in an inhibition zone measurement of 0 mm. The measurement of inhibition zones is directly related to the concentration of synthesized materials. The increase in the concentration of doped material leads to an enhancement in the inhibition zones associated with the corresponding increase in the surface area and porosity of NWs. The surface area and porosity increased the antimicrobial activity as the sharp edge of NWs penetrated the bacterial membrane effectively, resulting in bacterial death.[62] Upon the incorporation of Ag/C$_3$N$_4$ and C$_3$N$_4$/Ag, the enhanced antimicrobial activity is attributed to Ag, which acts as an electron pool and generates electrons and holes pair and produces the active species due to the surface plasmon effect of Ag.[33] The prepared catalysts were used for antimicrobial potential as antibacterial drugs, healthcare facility surfaces, promote healing and protect the wound from further harm and illuminate water-borne diseases, which help to avoid infections.[63]

To investigate the antimicrobial inhibition zones, a comparison graph was conducted between high and low concentrations of synthesized NWs and positive control (Fig. 10(a)). The percentage efficacy for S. aureus was determined using relation (5).

$$\text{Efficacy } (\%) = \frac{\text{sample inhibation zone}}{\text{positive control inhibation zone}} \times 100 \quad (5)$$

The measured results (Fig. 10(b)) illustrate a significant enhancement in efficacy in the range of 19.12–42.62% at low and 36.61–49.72% at high concentrations for pure, Ag/C$_3$N$_4$ and C$_3$N$_4$/Ag doped NiSe NWs against MDR S. aureus isolated from bovine mastitis. Overall, the synthesized C$_3$N$_4$/Ag-doped NiSe NWs depicted maximum bactericidal response and presented a future antibiotic placebo to treat MDR S. aureus infections, leading to bovine mastitis. The synthesized materials acted as antibacterial agents that kill pathogenic microorganisms without the side effects. In the practical field, the concentration

**Table 2** Antibacterial efficacy of NiSe and Ag/C$_3$N$_4$, and C$_3$N$_4$/Ag-doped NiSe

| | Inhibition zones (mm) | |
| --- | --- | --- |
| Samples | 0.5 mg/50 μL | 1.0 mg/50 μL |
| NiSe | 1.75 | 3.35 |
| Ag/C$_3$N$_4$-doped NiSe | 2.65 | 3.85 |
| C$_3$N$_4$/Ag-doped NiSe | 3.90 | 4.55 |
| Ciprofloxacin | 9.15 | 9.15 |
| DI water | 0 | 0 |
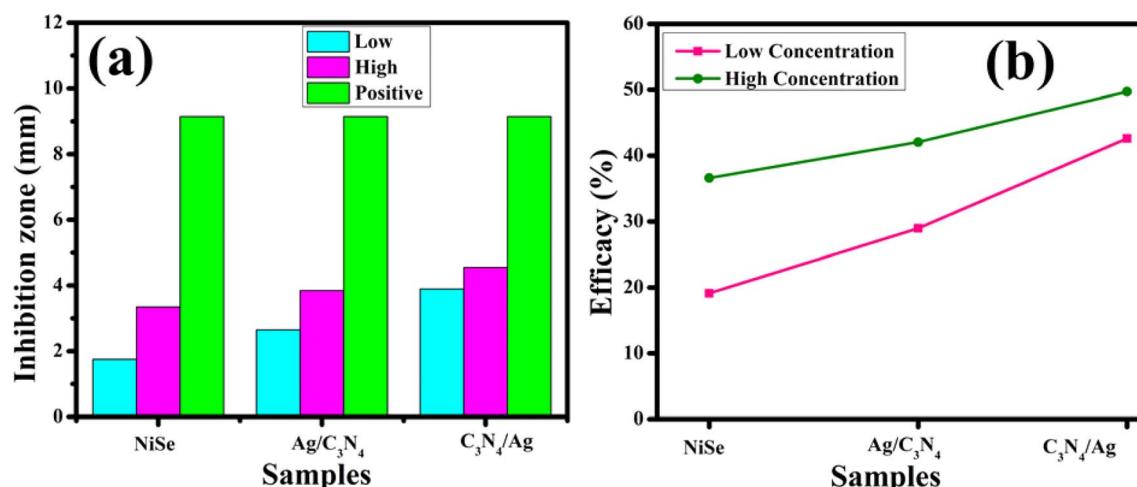


Fig. 10 Graphical investigation of inhibition zone measurement: (a) inhibition zone comparison and (b) % age efficiency of NiSe, Ag/C$_3$N$_4$ and C$_3$N$_4$/Ag-doped NiSe doped NiSe for S. aureus.

**Table 3** Literature comparison of the antimicrobial activity

| Samples | Standard drug | Bacteria | Inhibition zones (mm) | | Concentration dose of materials | Ref. |
| --- | --- | --- | --- | --- | --- | --- |
| | | | Catalyst | +ve control | | |
| NiSe | Gentamycin | E. coli | 10 | 18 | 5 mL | 7 |
| NiSe | Gentamycin | S. aureus | 15 | 18 | 5 mL | 7 |
| NiSe | Ciprofloxacin | S. aureus | 3.35 | 9.15 | 1.0 mg/50 μL | Present study |
| C$_3$N$_4$/Ag-doped NiSe | Ciprofloxacin | S. aureus | 4.55 | 9.15 | 1.0 mg/50 μL | Present study |

© 2024 The Author(s). Published by the Royal Society of Chemistry

RSC Adv., 2024, **14**, 20004–20019 | **20013**
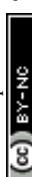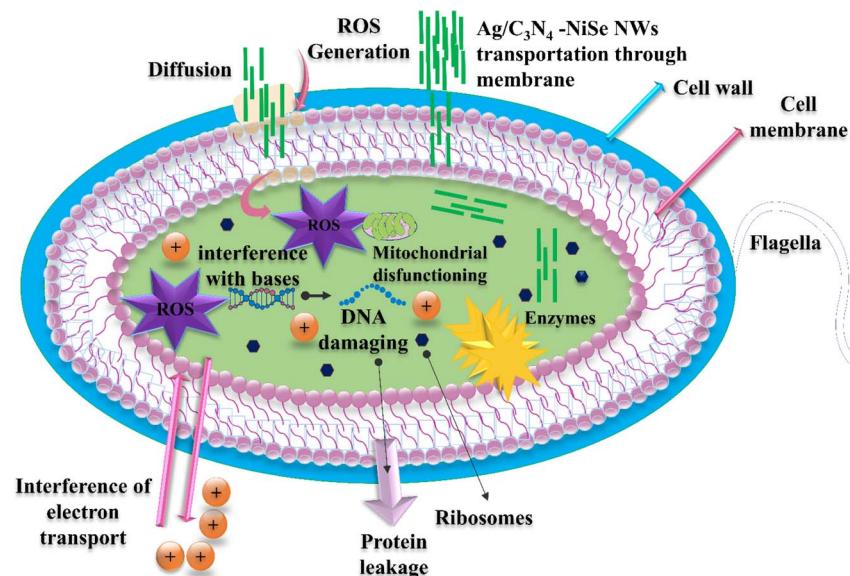
Fig. 11  Schematic illustration mechanism for bacterial death.

doses affect human and animal life; thus, it is essential to determine the optimum materials concentration to achieve the appropriate efficacy against MDR *S. aureus*. Bacterial responses to drugs are concentration-dependent. Antibiotics have

antimicrobial effects on sensitive cells at high concentrations, whereas sub-inhibitory doses cause a variety of biological responses in bacteria. Higher concentration doses may provide effective bacterial death and control.[64] The literature
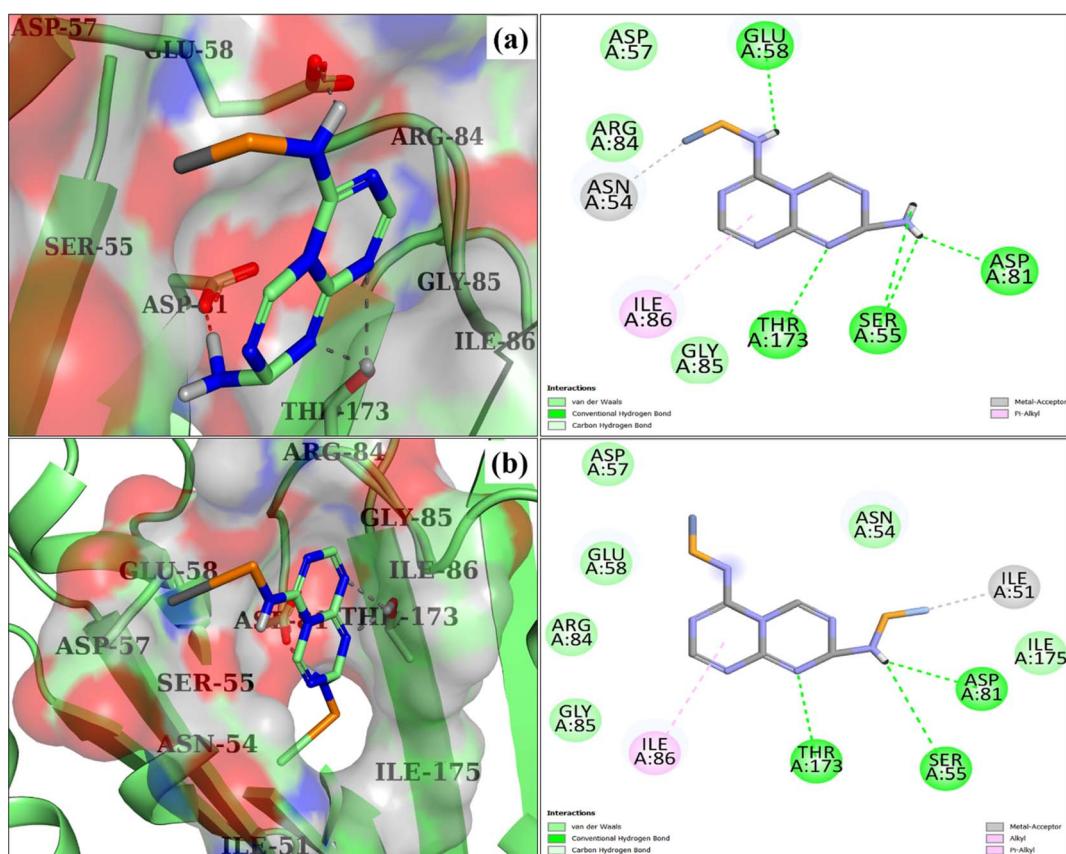


Fig. 12  3D and 2D depiction of the binding interaction pattern inside the active site of DNA gyrase$_{S.\ aureus}$: (a) $C_3N_4$/Ag-doped NiSe and (b) Ag/$C_3N_4$-doped NiSe.

comparison of inhibition zone measurement using NiSe as a catalyst using gentamycin as the positive control achieves significant achievement for bacterial death. In the present research, low and high concentration doses have been used to control and kill the microorganism, as represented in Table 3.

The small-sized particles are responsible for the production of reactive oxygen species (ROS). Electron–hole pairs are the main facilitators in the production of ROS such as the superoxide anion radical ($*O_2^-$), hydroxyl radical ($*OH$), and hydrogen peroxide radicals ($*H_2O_2$). ROS production is revealed in the reaction mechanism eqn (6)–(11) and is represented in Fig. 11.

$$NWs + h\nu \text{ (photon)} \rightarrow h^+ + e^- \tag{6}$$

$$e^- + O_2 \rightarrow *O_2^- \tag{7}$$

$$h^+ + H_2O \rightarrow OH^- + H^+ \tag{8}$$

$$*O_2^- + H^+ \rightarrow *HO_2 \tag{9}$$

$$*HO_2 + e^- + H^+ \rightarrow *H_2O_2 \tag{10}$$

$$*H_2O_2 + *O_2^- \rightarrow *OH + O_2 + OH^- \tag{11}$$
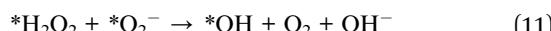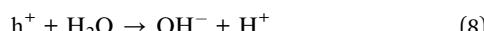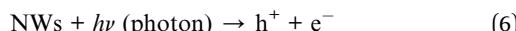
The hydrogen peroxide radical ($*H_2O_2$) causes substantial harm to bacterial cells, resulting in the death of bacteria.[65] The rate at which radicals are produced can greatly impact the antibacterial activities by increasing the level of induced oxidative stress.[66] The cell wall of *S. aureus* consists of a thin layer of peptidoglycan and teichoic acid with pores on the surface of the bacterial cell. The existence of these pores enables the penetration of external substances into the cell wall, leading to the death of bacterial cells. $C_3N_4$ and Ag-doped NiSe materials produce ROS that penetrate the bacterial cells and react with DNA and proteins, leading to the damage of the bacterial cell. Multiple studies have suggested that the antibacterial effectiveness of NiSe is related to various factors such as their size, surface area, shape, and the surface charge of the synthesized materials. Additionally, the particular strains of bacteria and the surrounding environmental factors affect the antibacterial effectiveness.[7,67]

### 3.12. Molecular docking studies

Computational strategies, notably molecular docking studies,[68] have garnered a lot of attention in recent years, and there is uncertainty in the extensive analysis of the mechanisms behind many biological processes.[69] In this study, molecular docking was used to find prospective enzyme inhibitors by evaluating their binding affinity and inhibitory capacity with respect to NWs. Enzymes DDI and DNA gyrase, crucial for bacterial survival and development, have been recognized as significant targets in the quest for antibiotics.[70,71] The optimal docking
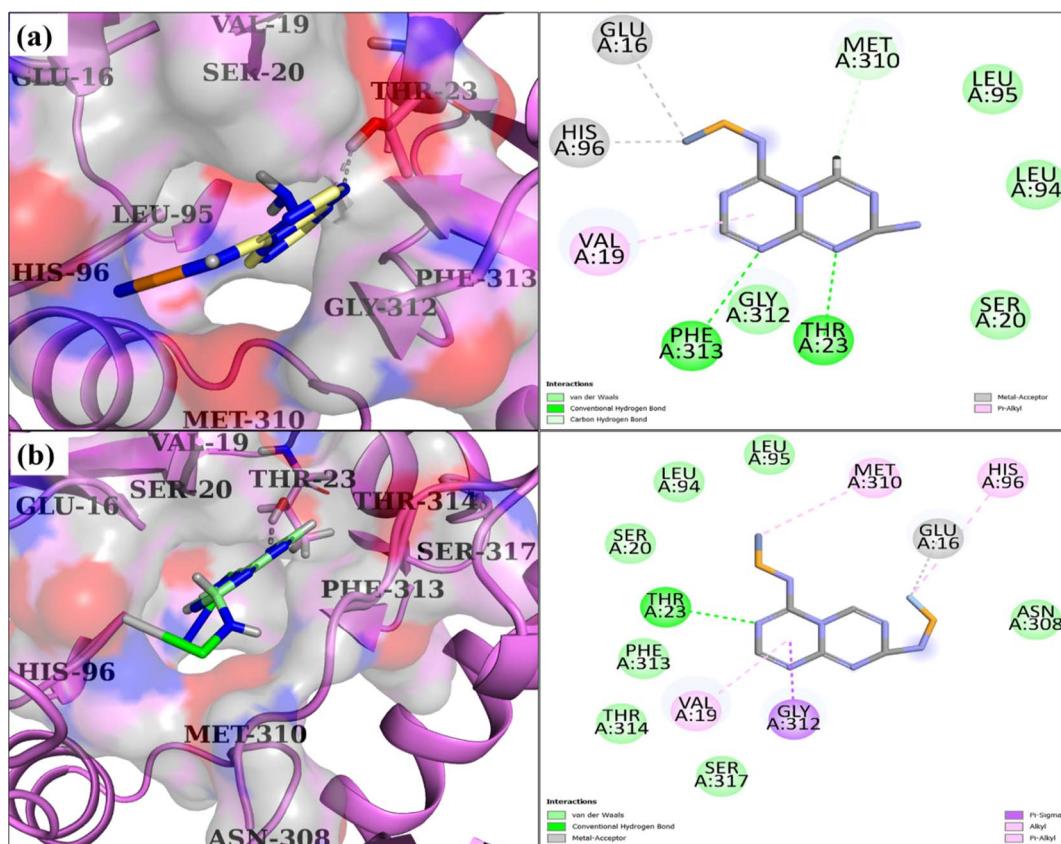


**Fig. 13** 3D and 2D depiction of the binding interaction pattern inside the active site of DDI$_{S. aureus}$: (a) $C_3N_4$/Ag-doped NiSe and (b) Ag/$C_3N_4$-doped NiSe.

conformation of $C_3N_4$-doped NiSe, as indicated by a binding score of 4.61, exhibited hydrogen bonding with Ser55, Glu58, Asp81, and Thr173, pi–alkyl interactions for Ile86, and metal acceptor interactions with Asn54 of DNA gyrase, as indicated in Fig. 12(a). In contrast, the Ag/$C_3N_4$-doped NiSe compound demonstrated a pi–alkyl linkage to Ile86, a metal acceptor affinity for Ile51, and hydrogen bonding interactions with Ser55, Asp81, and Thr173. These interactions resulted in a docking score of 5.73, as seen in Fig. 12(b).

Furthermore, it has been found that $C_3N_4$/Ag-doped NiSe forms hydrogen bonds with Thr23 and Phe313, acts as a metal acceptor with Glu16 and His96, and engages in pi–alkyl interactions with Val19 of DDl, having a binding score of 3.89, as represented in Fig. 13(a). The Ag/$C_3N_4$-doped NiSe structure in its optimal docking conformation exhibited many noteworthy interactions. Specifically, it formed hydrogen bonds with Thr23, engaged in pi–sigma interactions with Gly312, metal acceptor connections with Glu16, and participated in pi–alkyl interactions with Val19, His96, and Met310 along with a binding score of 4.28, as seen in Fig. 13(b).

The *in silico* and antibacterial activities are comparable, suggesting that Ag/$C_3N_4$-doped NiSe are potential inhibitors for DDl and DNA gyrase from *S. aureus* that need additional investigation.

## 4  Conclusion

In this research, NiSe, Ag/$C_3N_4$ and $C_3N_4$/Ag-doped NiSe were synthesized using the coprecipitation method to improve the catalytic, bactericidal activity and *in silico* docking study. The crystalline size, surface area, and porosity of synthesized NWs were investigated using XRD analysis. The crystalline size decreased, and the surface area (40.95–50.72 m$^2$ g$^{-1}$) and the porosity (4–34.1%) of NWs increased with the incorporation of $C_3N_4$/Ag and Ag/$C_3N_4$. TEM micrographs confirmed the NWs-like morphology of the synthesized material. Ag/$C_3N_4$-doped NiSe NWs exhibit efficient catalytic degradation (69.58%) of the RhB dye in a basic medium. The antimicrobial efficiency was measured as (1.75–3.90 mm) and (3.35–4.55 mm) at low and high concentrations of NWs, respectively. The potential inhibitory effects of the produced NWs on the DDl and DNA gyrase enzymes of *S. aureus* were investigated by molecular docking analysis, which indicates that Ag/$C_3N_4$-doped NiSe NWs are potential inhibitors of DNA gyrase and DDl. Experimental consequences demonstrate that the synthesized NWs effectively eliminate toxic industrial effluents and cause the death of pathogenic bacteria, leading to their potential future applications.

## Data availability

The data are available upon reasonable request.

## Conflicts of interest

The authors declare no conflict of interest.

## Acknowledgements

## References

1 L. Du, W. Du, H. Ren, N. Wang, Z. Yao, X. Shi, B. Zhang, J. Zai and X. Qian, Honeycomb-like metallic nickel selenide nanosheet arrays as binder-free electrodes for high-performance hybrid asymmetric supercapacitors, *J. Mater. Chem. A*, 2017, **5**, 22527–22535, DOI: 10.1039/c7ta06921a.

2 R. Maryam, M. Arif, R. Hussain, B. A. Khan, A. Shah, R. Ahmad, A. Mahmood, Z. U. Shah and S. ur Rahman, Enhanced photocatalytic and antibacterial activity of NiSe$_2$–TiO$_2$ nanocomposites under visible light, *Opt. Mater.*, 2023, **143**, 114183, DOI: 10.1016/j.optmat.2023.114183.

3 M. A. Park, Y. Chang, I. Choi, J. Bai, N. Ja-hyun and J. Han, Development of A Comprehensive Biological Hazard-Proof Packaging Film with Insect-Repellent, Antibacterial, and Antifungal Activities, *J. Food Sci.*, 2018, **83**, 3035–3043, DOI: 10.1111/1750-3841.14397.

4 F. Gomes and M. Henriques, Control of Bovine Mastitis: Old and Recent Therapeutic Approaches, *Curr. Microbiol.*, 2016, **72**, 377–382, DOI: 10.1007/s00284-015-0958-8.

5 X. Zhao and P. Lacasse, Mammary tissue damage during bovine mastitis: causes and control, *J. Anim. Sci.*, 2008, **86**, 57–65, DOI: 10.2527/jas.2007-0302.

6 Y. N. Slavin, J. Asnis, U. O. Häfeli and H. Bach, Metal nanoparticles: understanding the mechanisms behind antibacterial activity, *J. Nanobiotechnol.*, 2017, **15**, 65, DOI: 10.1186/s12951-017-0308-z.

7 L. Velayutham, C. Parvathiraja, D. C. Anitha, K. Mahalakshmi, M. Jenila, J. K. Gupta, S. M. Wabaidur, M. R. Siddiqui, S. Aftab and W. C. Lai, Antibacterial and Photocatalytic Dye Degradation Activities of Green Synthesized NiSe Nanoparticles from Hibiscus rosa-sinensis Leaf Extract, *Water*, 2023, **15**, 1380, DOI: 10.3390/w15071380.

8 M. Mon, R. Bruno, E. Tiburcio, M. Viciano-Chumillas, L. H. G. Kalinke, J. Ferrando-Soria, D. Armentano and E. Pardo, Multivariate Metal-Organic Frameworks for the Simultaneous Capture of Organic and Inorganic Contaminants from Water, *J. Am. Chem. Soc.*, 2019, **141**, 13601–13609, DOI: 10.1021/jacs.9b06250.

9 S. S. Affat, Classifications, Advantages, Disadvantages, Toxicity Effects of Natural and Synthetic Dyes: A Review, *University of Thi-Qar Journal of Science*, 2021, **8**, 130–135, DOI: 10.32792/utq/utjsci/v8/1/21.

10 S. Rahdar, A. Rahdar, M. N. Zafar, S. S. Shafqat and S. Ahmadi, Synthesis and characterization of MgO supported Fe-Co-Mn nanoparticles with exceptionally high

adsorption capacity for rhodamine B dye, *J. Mater. Res. Technol.*, 2019, **8**, 3800–3810, DOI: **10.1016/j.jmrt.2019.06.041**.

11  H. A. Elbadawy, A. F. Elhusseiny, S. M. Hussein and W. A. Sadik, Sustainable and energy-efficient photocatalytic degradation of textile dye assisted by ecofriendly synthesized silver nanoparticles, *Sci. Rep.*, 2023, **13**, 2302, DOI: **10.1038/s41598-023-29507-x**.

12  S. Kaushal, P. Pal Singh and N. Kaur, Metal organic framework-derived Zr/Cu bimetallic photocatalyst for the degradation of tetracycline and organic dyes, *Environ. Nanotechnol., Monit. Manage.*, 2022, **18**, 100727, DOI: **10.1016/j.enmm.2022.100727**.

13  M. T. Ameen, A. Haider, I. Shahzadi, A. Shahbaz, A. Ul-Hamid, H. Ullah, S. Khan and M. Ikram, Exploring catalytic efficacy and anti-bacterial performance with molecular docking analysis of g-C$_3$N$_4$-grafted-Ag doped SnO$_2$ QDs, *Res. Chem. Intermed.*, 2024, 1–18, DOI: **10.1007/s11164-024-05241-5**.

14  M. Khan, A. Khan, H. Khan, N. Ali, S. Sartaj, S. Malik, N. Ali, H. Khan, S. Shah and M. Bilal, Development and characterization of regenerable chitosan-coated nickel selenide nano-photocatalytic system for decontamination of toxic azo dyes, *Int. J. Biol. Macromol.*, 2021, **182**, 866–878, DOI: **10.1016/j.ijbiomac.2021.03.192**.

15  R. Divya, N. Manikandan and G. Vinitha, Synthesis and characterization of nickel doped zinc selenide nanospheres for nonlinear optical applications, *J. Alloys Compd.*, 2019, **791**, 601–612, DOI: **10.1016/j.jallcom.2019.03.294**.

16  G. S. Tito, A. S. Abolanle, A. T. Kuvarega, A. O. Idris, B. B. Mamba and U. Feleni, Nickel Selenide Quantum Dot Applications in Electrocatalysis and Sensors, *Electroanalysis*, 2020, **32**, 2603–2614, DOI: **10.1002/elan.202060341**.

17  M. V. V. T. Poiyamozhi and J. Thivya, Design and fabrication of graphitic carbon nitride incorporated nickel selenide hybrid composite for effective degradation of organic pollutants under UV and natural sunlight irradiations, *Diamond Relat. Mater.*, 2024, **142**, 110726, DOI: **10.1016/j.diamond.2023.110726**.

18  A. Malankowska, A. Mikołajczyk, J. Mędrzycka, I. Wysocka, G. Nowaczyk, M. Jarek, T. Puzyn and E. Mulkiewicz, The effect of Ag, Au, Pt, and Pd on the surface properties, photocatalytic activity and toxicity of multicomponent TiO$_2$-based nanomaterials, *Environ. Sci.: Nano*, 2020, **7**, 3557–3574, DOI: **10.1039/d0en00580k**.

19  M. Azami, M. Haghighi and S. Allahyari, Sono-precipitation of Ag$_2$CrO$_4$-C composite enhanced by carbon-based materials (AC, GO, CNT and C$_3$N$_4$) and its activity in photocatalytic degradation of acid orange 7 in water, *Ultrason. Sonochem.*, 2018, **40**, 505–516, DOI: **10.1016/j.ultsonch.2017.07.043**.

20  M. K. Ahmed, A. E. Shalan, M. Afifi, M. M. El-Desoky and S. Lanceros-Méndez, Correction: Silver-doped cadmium selenide/graphene oxide-filled cellulose acetate nanocomposites for photocatalytic degradation of

malachite green toward wastewater treatment, *ACS Omega*, 2022, **7**, 18190–18191, DOI: **10.1021/acsomega.2c02634**.

21  F. A. Zhao, H. Y. Xiao, X. M. Bai and X. T. Zu, Effects of Ag doping on the electronic and optical properties of CdSe quantum dots, *Phys. Chem. Chem. Phys.*, 2019, **21**, 16108–16119, DOI: **10.1039/c9cp02433f**.

22  J. C. Wang, C. X. Cui, Y. Li, L. Liu, Y. P. Zhang and W. Shi, Porous Mn doped g-C$_3$N$_4$ photocatalysts for enhanced synergetic degradation under visible-light illumination, *J. Hazard. Mater.*, 2017, **339**, 43–53, DOI: **10.1016/j.jhazmat.2017.06.011**.

23  G. Mamba and A. K. Mishra, Graphitic carbon nitride (g-C$_3$N$_4$) nanocomposites: a new and exciting generation of visible light driven photocatalysts for environmental pollution remediation, *Appl. Catal., B*, 2016, **198**, 347–377, DOI: **10.1016/j.apcatb.2016.05.052**.

24  M. Rani, M. Murtaza, A. Amjad, M. Zahra, A. Waseem and A. Alhodaib, NiSe$_2$/Ag$_3$PO$_4$ Nanocomposites for Enhanced Visible Light Photocatalysts for Environmental Remediation Applications, *Catalysts*, 2023, **13**, 929, DOI: **10.3390/catal13060929**.

25  M. Aadil, M. Mahmood, M. F. Warsi, I. A. Alsafari, S. Zulfiqar and M. Shahid, Fabrication of MnO$_2$ nanowires and their nanohybrid with flat conductive matrix for the treatment of industrial effluents, *FlatChem*, 2021, **30**, 100316, DOI: **10.1016/j.flatc.2021.100316**.

26  M. Altaf, M. Ijaz, A. Ghaffar, A. Rehman and M. Avais, Antibiotic susceptibility profile and synergistic effect of non-steroidal anti-inflammatory drugs on antibacterial activity of resistant antibiotics (oxytetracycline and gentamicin) against methicillin resistant *Staphylococcus aureus* (MRSA), *Microb. Pathog.*, 2019, **137**, 103755, DOI: **10.1016/j.micpath.2019.103755**.

27  B. A. Iwalokun, A. Ogunledun, D. O. Ogbolu, S. B. Bamiro and J. Jimi-Omojola, *In vitro* antimicrobial properties of aqueous garlic extract against multidrug-resistant bacteria and *Candida* species from Nigeria, *J. Med. Food*, 2004, **7**, 327–333, DOI: **10.1089/jmf.2004.7.327**.

28  S. Liu, J. S. Chang, J. T. Herberg, M. M. Horng, P. K. Tomich, A. H. Lin and K. R. Marotti, Allosteric inhibition of *Staphylococcus aureus* D-alanine:D-alanine ligase revealed by crystallographic studies, *Proc. Natl. Acad. Sci. U. S. A.*, 2006, **103**, 15178–15183, DOI: **10.1073/pnas.0604905103**.

29  M. F. Mesleh, J. B. Cross, J. Zhang, J. Kahmann, O. A. Andersen, J. Barker, R. K. Cheng, B. Felicetti, M. Wood, A. T. Hadfield, C. Scheich, T. I. Moy, Q. Yang, J. Shotwell, K. Nguyen, B. Lippa, R. Dolle and M. D. Ryan, Fragment-based discovery of DNA gyrase inhibitors targeting the ATPase subunit of GyrB, *Bioorg. Med. Chem. Lett.*, 2016, **26**, 1314–1318, DOI: **10.1016/j.bmcl.2016.01.009**.

30  I. Shahzadi, M. Islam, H. Saeed, A. Haider, A. Shahzadi, J. Haider, N. Ahmed, A. Ul-Hamid, W. Nabgan, M. Ikram and H. A. Rathore, Formation of biocompatible MgO/cellulose grafted hydrogel for efficient bactericidal and controlled release of doxorubicin, *Int. J. Biol. Macromol.*, 2022, **220**, 1277–1286, DOI: **10.1016/j.ijbiomac.2022.08.142**.

31 K. Rehman, T. A. Chohan, I. Waheed, Z. Gilani and M. S. H. Akash, Taxifolin prevents postprandial hyperglycemia by regulating the activity of α-amylase: evidence from an *in vivo* and *in silico* studies, *J. Cell. Biochem.*, 2019, **120**, 425–438, DOI: **10.1002/jcb.27398**.

32 W. Welch, J. Ruppert and A. N. Jain, Hammerhead: fast, fully automated docking of flexible ligands to protein binding sites, *Chem. Biol.*, 1996, **3**, 449–462, DOI: **10.1016/S1074-5521(96)90093-9**.

33 X. Bai, R. Zong, C. Li, D. Liu, Y. Liu and Y. Zhu, Enhancement of visible photocatalytic activity *via* Ag@C$_3$N$_4$ core-shell plasmonic composite, *Appl. Catal., B*, 2014, **147**, 82–91, DOI: **10.1016/j.apcatb.2013.08.007**.

34 R. C. Ngullie, S. O. Alaswad, K. Bhuvaneswari, P. Shanmugam, T. Pazhanivel and P. Arunachalam, Synthesis and characterization of efficient ZnO/g-C$_3$N$_4$ nanocomposites photocatalyst for photocatalytic degradation of methylene blue, *Coatings*, 2020, **10**, 500, DOI: **10.3390/COATINGS10050500**.

35 M. Aadil, A. G. Taki, S. Zulfiqar, A. Rahman, M. Shahid, M. F. Warsi, Z. Ahmad, A. A. Alothman and S. Mohammad, Gadolinium doped zinc ferrite nanoarchitecture reinforced with a carbonaceous matrix: a novel hybrid material for next-generation flexible capacitors, *RSC Adv.*, 2023, **13**, 28063–28075, DOI: **10.1039/d3ra05290g**.

36 M. Rashid, W. Hassan, M. Aadil, H. H. Somaily, N. M. Mahdi, R. Lataef, A. G. Taki, K. Srithilat, D. F. Baamer, S. M. Albukhari, M. A. Salam and A. Llyas, Solar-light-driven and magnetically recoverable doped nano-ferrite: an ideal photocatalyst for water purification applications, *Opt. Mater.*, 2023, **135**, 113192, DOI: **10.1016/j.optmat.2022.113192**.

37 S. Majumdar, The effects of crystallite size, surface area and morphology on the sensing properties of nanocrystalline SnO$_2$ based system, *Ceram. Int.*, 2015, **41**, 14350–14358, DOI: **10.1016/j.ceramint.2015.07.068**.

38 M. Aadil, W. Hassan, H. H. Somaily, S. R. Ejaz, R. R. Abass, H. Jasem, S. K. Hachim, A. H. Adhab, E. S. Abood and I. A. Alsafari, Synergistic effect of doping and nanotechnology to fabricate highly efficient photocatalyst for environmental remediation, *J. Alloys Compd.*, 2022, **920**, 165876, DOI: **10.1016/j.jallcom.2022.165876**.

39 M. Rashid, S. Parsaei, A. Ghoorchian, K. Dashtian and D. Mowla, A spiral shape microfluidic photoreactor with MOF(NiFe)-derived NiSe-Fe$_3$O$_4$/C heterostructure for photodegradation of tetracycline: mechanism conception and DFT calculation, *J. Ind. Eng. Chem.*, 2023, **121**, 275–286, DOI: **10.1016/j.jiec.2023.01.031**.

40 I. O. Faniyi, O. Fasakin, B. Olofinjana, A. S. Adekunle, T. V Oluwasusi, M. A. Eleruja and E. O. B. Ajayi, The comparative analyses of reduced graphene oxide (RGO) prepared *via* green, mild and chemical approaches, *SN Appl. Sci.*, 2019, **1**, 1–7, DOI: **10.1007/s42452-019-1188-7**.

41 S. Saranya, S. Dhanapandian, S. Nagarajan, S. Suthakaran and N. Krishnakumar, Hydrothermal synthesis and characterization of nanostructured nickel diselenide (NiSe$_2$) from the decomposition of nickel acetate tetrahydrate (Ni(CH$_3$COO)$_2$)·4H$_2$O, *Mater. Lett.*, 2020, **277**, 128398, DOI: **10.1016/j.matlet.2020.128398**.

42 H. Jiang, Z. Wang, Q. Yang, L. Tan, L. Dong and M. Dong, Ultrathin Ti$_3$C$_2$T$_x$ (MXene) Nanosheet-Wrapped NiSe$_2$ Octahedral Crystal for Enhanced Supercapacitor Performance and Synergetic Electrocatalytic Water Splitting, *Nano-Micro Lett.*, 2019, **11**, 1–14, DOI: **10.1007/s40820-019-0261-5**.

43 R. Chellappa, D. Dattelbaum, L. Daemen and Z. Liu, High pressure spectroscopic studies of hydrazine (N$_2$H$_4$), *J. Phys.: Conf. Ser.*, 2014, **500**, 052008, DOI: **10.1088/1742-6596/500/5/052008**.

44 L. Zhang, T. Wang, L. Sun, Y. Sun, T. Hu, K. Xu and F. Ma, Hydrothermal synthesis of 3D hierarchical MoSe$_2$/NiSe$_2$ composite nanowires on carbon fiber paper and their enhanced electrocatalytic activity for the hydrogen evolution reaction, *J. Mater. Chem. A*, 2017, **5**, 19752–19759, DOI: **10.1039/c7ta05352e**.

45 D. Liang, J. Mao, P. Liu, J. Li, J. Yan and W. Song, *In situ* doping of Co in nickel selenide nanoflower for robust electrocatalysis towards oxygen evolution, *Int. J. Hydrogen Energy*, 2020, **45**, 27047–27055, DOI: **10.1016/j.ijhydene.2020.07.017**.

46 S. Anantharaj, J. Kennedy and S. Kundu, Microwave-Initiated Facile Formation of Ni$_3$Se$_4$ Nanoassemblies for Enhanced and Stable Water Splitting in Neutral and Alkaline Media, *ACS Appl. Mater. Interfaces*, 2017, **9**, 8714–8728, DOI: **10.1021/acsami.6b15980**.

47 J. Dong, J. Wu, J. Jia, L. Fan and J. Lin, Nickel selenide/reduced graphene oxide nanocomposite as counter electrode for high efficient dye-sensitized solar cells, *J. Colloid Interface Sci.*, 2017, **498**, 217–222, DOI: **10.1016/j.jcis.2017.03.025**.

48 N. Moloto, M. J. Moloto, N. J. Coville and S. Sinha Ray, Optical and structural characterization of nickel selenide nanoparticles synthesized by simple methods, *J. Cryst. Growth*, 2009, **311**, 3924–3932, DOI: **10.1016/j.jcrysgro.2009.06.006**.

49 F. Nie, Z. Li, X. Dai, X. Yin, Y. Gan, Z. Yang, B. Wu, Z. Ren, Y. Cao and W. Song, Interfacial electronic modulation on heterostructured NiSe@CoFe LDH nanoarrays for enhancing oxygen evolution reaction and water splitting by facilitating the deprotonation of OH to O, *Chem. Eng. J.*, 2022, **431**, 134080, DOI: **10.1016/j.cej.2021.134080**.

50 M. Salavati-Niasari and A. Sobhani, Effect of nickel salt precursors on morphology, size, optical property and type of products (NiSe or Se) in hydrothermal method, *Opt. Mater.*, 2013, **35**, 904–909, DOI: **10.1016/j.optmat.2012.11.004**.

51 M. S. Begum and A. J. Ahamed, Synthesis and Characterization of Chromium Doped NiSe, *J. Environ. Nanotechnol.*, 2015, **4**, 6–11, DOI: **10.13074/jent.2015.09.153156**.

52 F. Amano, K. Nogami, M. Tanaka and B. Ohtani, Correlation between surface area and photocatalytic activity for acetaldehyde decomposition over bismuth tungstate

particles with a hierarchical structure, *Langmuir*, 2010, **26**, 7174–7180, DOI: **10.1021/la904274c**.

53 S. S. Mohtar, F. Aziz, A. F. Ismail, N. S. Sambudi, H. Abdullah, A. N. Rosli and B. Ohtani, Impact of doping and additive applications on photocatalyst textural properties in removing organic pollutants: a review, *Catalysts*, 2021, **11**, 1160, DOI: **10.3390/catal11101160**.

54 R. tang Guo, J. Wang, Z. xu Bi, X. Chen, X. Hu and W. guo Pan, Recent advances and perspectives of g-C$_3$N$_4$-based materials for photocatalytic dyes degradation, *Chemosphere*, 2022, **295**, 133834, DOI: **10.1016/j.chemosphere.2022.133834**.

55 S. Shen, H. Zhang, A. Xu, Y. Y. Zhao, Z. Lin, Z. Wang, W. Zhong and S. Feng, Construction of NiSe$_2$/BiVO$_4$ Schottky junction derived from work function discrepancy for boosting photocatalytic activity, *J. Alloys Compd.*, 2021, **875**, 160071, DOI: **10.1016/j.jallcom.2021.160071**.

56 Z. Chen, Y. Gao, F. Chen and H. Shi, Metallic NiSe cocatalyst decorated g-C$_3$N$_4$ with enhanced photocatalytic activity, *Chem. Eng. J.*, 2021, **413**, 127474, DOI: **10.1016/j.cej.2020.127474**.

57 K. Mahalakshmi, R. Mary Jenila, I. Vetha Potheher, V. Lakshmi and V. Thangaraj, Bifunctional rGO incorporated NiSe$_2$ nanocomposite as a photocatalyst and an electrode in supercapacitor, *J. Alloys Compd.*, 2024, **972**, 172699, DOI: **10.1016/j.jallcom.2023.172699**.

58 A. Kanwal, T. Shahzadi, T. Riaz, M. Zaib, S. Khan, M. A. Habila and M. Sillanpaa, Photocatalytic Degradation Studies of Organic Dyes over Novel Cu/Ni Loaded Reduced Graphene Oxide Hybrid Nanocomposite: Adsorption, Kinetics and Thermodynamic Studies, *Molecules*, 2023, **28**, 6474, DOI: **10.3390/molecules28186474**.

59 L. Hu, H. Yuan, L. Zou, F. Chen and X. Hu, Adsorption and visible light-driven photocatalytic degradation of rhodamine B in aqueous solutions by Ag@AgBr/SBA-15, *Appl. Surf. Sci.*, 2015, **355**, 706–715, DOI: **10.1016/j.apsusc.2015.04.166**.

60 Y. Cai, Y. Luo, B. C. Sun, T. X. Fan, G. W. Chu and J. F. Chen, A novel plasma-assisted rotating disk reactor: enhancement of degradation efficiency of rhodamine B, *Chem. Eng. J.*, 2019, **377**, 119897, DOI: **10.1016/j.cej.2018.09.058**.

61 D. Xu, X. Sun, X. Zhao, L. Huang, Y. Qian, X. Tao and Q. Guo, Heterogeneous Fenton Degradation of Rhodamine B in Aqueous Solution Using Fe-Loaded Mesoporous MCM-41 as Catalyst, *Water, Air, Soil Pollut.*, 2018, **229**, 1–9, DOI: **10.1007/s11270-018-3932-9**.

62 L. Liu, S. Chen, X. Zhang, Z. Xue, S. Cui, X. Hua, B. Yang, H. Yan, C. Liu, J. Wang, Z. Zhang, W. Yu, F. Wu, W. Xu, V. P. Lehto, T. Yue, Y. Liu, Y. Yu, T. Wang and J. Wang, Mechanical penetration of β-lactam-resistant Gram-negative bacteria by programmable nanowires, *Sci. Adv.*, 2020, **6**, eabb9593, DOI: **10.1126/SCIADV.ABB9593**.

63 Y. Liang, Y. Liang, H. Zhang and B. Guo, Antibacterial biomaterials for skin wound dressing, *Asian J. Pharm. Sci.*, 2022, **17**, 353–384, DOI: **10.1016/j.ajps.2022.01.001**.

64 S. P. Bernier and M. G. Surette, Concentration-dependent activity of antibiotics in natural environments, *Front. Microbiol.*, 2013, **4**, 20, DOI: **10.3389/fmicb.2013.00020**.

65 Z. N. Kayani, M. Sahar, S. Riaz, S. Naseem and Z. Saddiqe, Enhanced magnetic, antibacterial and optical properties of Sm doped ZnO thin films: role of Sm doping, *Opt. Mater.*, 2020, **108**, 110457, DOI: **10.1016/j.optmat.2020.110457**.

66 N. Rajiv Chandar, S. Agilan, R. Thangarasu, N. Muthukumarasamy, J. Chandrasekaran, S. Arunachalam and S. R. Akshaya, Elucidation of efficient dual performance in photodegradation and antibacterial activity by a promising candidate Ni-doped MoO$_3$ nanostructure, *J. Sol-Gel Sci. Technol.*, 2021, **100**, 451–465, DOI: **10.1007/s10971-020-05382-0**.

67 G. K. Jhanani, M. M. Al-Ansari, R. M, J. Lee, E. Sathiyamoorthi and I. Karuppusamy, Photocatalytic removal of benzo[a]pyrene and antibacterial efficacy of graphitic carbon nitride-silver-nickel (g-C$_3$N$_4$–Ag–Ni) mediated nanocomposites, *Chemosphere*, 2024, **350**, 141122, DOI: **10.1016/j.chemosphere.2024.141122**.

68 A. V. Singh, M. Varma, M. Rai, S. Pratap Singh, G. Bansod, P. Laux and A. Luch, Advancing Predictive Risk Assessment of Chemicals *via* Integrating Machine Learning, Computational Modeling, and Chemical/Nano-Quantitative Structure-Activity Relationship Approaches, *Adv. Intell. Syst.*, 2024, **6**, 2300366, DOI: **10.1002/aisy.202300366**.

69 P. Abishad, P. Niveditha, V. Unni, J. Vergis, N. V. Kurkure, S. Chaudhari, D. B. Rawool and S. B. Barbuddhe, *In silico* molecular docking and *in vitro* antimicrobial efficacy of phytochemicals against multi-drug-resistant enteroaggregative *Escherichia coli* and non-typhoidal *Salmonella* spp, *Gut Pathog.*, 2021, **13**, 1–11, DOI: **10.1186/s13099-021-00443-3**.

70 Y. Qin, L. Xu, Y. Teng, Y. Wang and P. Ma, Discovery of novel antibacterial agents: recent developments in D-alanyl-D-alanine ligase inhibitors, *Chem. Biol. Drug Des.*, 2021, **98**, 305–322, DOI: **10.1111/cbdd.13899**.

71 S. J. McKie, K. C. Neuman and A. Maxwell, DNA topoisomerases: advances in understanding of cellular roles and multi-protein complexes *via* structure-function analysis, *BioEssays*, 2021, **43**, 2000286, DOI: **10.1002/bies.202000286**.